



# Isotropization and Evolution of Energy-containing Eddies in Solar Wind Turbulence: Parker Solar Probe, Helios 1, ACE, WIND, and Voyager 1

Manuel Enrique Cuesta<sup>1</sup> , Rohit Chhiber<sup>1,2</sup> , Sohom Roy<sup>1</sup> , Joshua Goodwill<sup>1</sup> , Francesco Pecora<sup>1</sup> , Jake Jarosik<sup>1</sup>, William H. Matthaeus<sup>1</sup> , Tulasi N. Parashar<sup>3</sup> , and Riddhi Bandyopadhyay<sup>4</sup>

<sup>1</sup> Department of Physics and Astronomy, Bartol Research Institut, University of Delaware, Newark, DE 19716, USA; [mecuesta@udel.edu](mailto:mecuesta@udel.edu)

<sup>2</sup> Heliophysics Science Division, NASA Goddard Space Flight Center, Greenbelt, MD 20771, USA

<sup>3</sup> School of Chemical and Physical Sciences, Victoria University of Wellington, Wellington, 6012, New Zealand

<sup>4</sup> Department of Astrophysical Sciences, Princeton University, Princeton, NJ 08544, USA

Received 2022 April 28; revised 2022 May 26; accepted 2022 May 27; published 2022 June 15

## Abstract

We examine the radial evolution of correlation lengths perpendicular ( $\lambda_C^\perp$ ) and parallel ( $\lambda_C^\parallel$ ) to the magnetic-field direction, computed from solar wind magnetic-field data measured by Parker Solar Probe (PSP) during its first eight orbits, Helios 1, Advanced Composition Explorer (ACE), WIND, and Voyager 1 spacecraft. Correlation lengths are grouped by an interval's alignment angle; the angle between the magnetic-field and solar wind velocity vectors ( $\Theta_{BV}$ ). Parallel and perpendicular angular channels correspond to angles  $0^\circ < \Theta_{BV} < 40^\circ$  and  $50^\circ < \Theta_{BV} < 90^\circ$ , respectively. We observe an anisotropy in the inner heliosphere within 0.40 au, with  $\lambda_C^\parallel / \lambda_C^\perp \approx 0.75$  at 0.10 au. This anisotropy reduces with increasing heliocentric distance and the correlation lengths roughly isotropize within 1 au. Results from ACE and WIND support a reversal of the anisotropy, such that  $\lambda_C^\parallel / \lambda_C^\perp \approx 1.29$  at 1 au. The ratio does not appear to change significantly beyond 1 au, although the small number of parallel intervals in the Voyager data set precludes unambiguous conclusions from being drawn. This study provides insights regarding the radial evolution of the large, most energetic interacting turbulent fluctuations in the heliosphere. We also emphasize the importance of tracking the changes in sampling direction in PSP measurements as the spacecraft approaches the Sun, when using these data to study the radial evolution of turbulence. This can prove to be vital in understanding the more complex dynamics of the solar wind in the inner heliosphere and can assist in improving related simulations.

*Unified Astronomy Thesaurus concepts:* Two-point correlation function (1951); Heliosphere (711); Solar wind (1534); Interplanetary turbulence (830)

## 1. Introduction

Plasma turbulence in the magnetohydrodynamic (MHD) regime has a well-known tendency to develop and sustain anisotropy relative to the mean magnetic-field direction (e.g., Oughton et al. 2015). This anisotropy has been extensively studied in observational, experimental, theoretical, and numerical works (e.g., Robinson & Rusbridge 1971; Shebalin et al. 1983; Matthaeus et al. 1990; Goldreich & Sridhar 1995; Dasso et al. 2005; Chhiber et al. 2020), and has significance for heliospheric plasma dynamics (DeForest et al. 2016), turbulence transport (Zank et al. 2021), and energetic particle scattering (Oughton & Engelbrecht 2021). Studies of anisotropy in the solar wind have most often concentrated on spectral (i.e., correlation) anisotropy or polarization (variance) anisotropy, in each case as measured in the inertial range (Oughton et al. 2015). Generally speaking, the larger, outer scale, or energy-containing eddies are expected to exhibit less anisotropy (Goldreich & Sridhar 1995). Nevertheless it is of interest to examine the dynamical development of outer-scale anisotropy, especially in Parker Solar Probe (PSP) spacecraft data (Fox et al. 2016), which may provide valuable insights concerning the dynamics of the young solar wind. Here we examine the radial evolution of large-scale anisotropies—at the

scale of the correlation length—as observed by PSP, complemented by other spacecraft at larger distances.

With each additional orbit, PSP compiles measurements of solar wind plasma in previously unexplored regions. In the inner heliosphere, the distinctive features of PSP's orbit implies sampling directions along the direction of bulk plasma flow in the spacecraft frame that differ from earlier spacecraft. The directions of the flow and the magnetic field as viewed by the spacecraft can be important when determining whether observed fluctuations of measured quantities are varying either parallel or perpendicular to the magnetic field. For a single spacecraft study such as this one, such restrictions on sampling directions are fundamental, since ideally we would like to simultaneously measure parallel and perpendicular correlations. We discuss this further in Section 5.

In the present study, the angle between the flow and magnetic-field vectors (alignment angle,  $\Theta_{BV}$ ) varies mainly due to the change in the heliospheric magnetic-field direction between PSP aphelia and perihelia, as well as the changes in the spacecraft velocity throughout the orbit. At greater distance from the Sun, the spacecraft speed is smaller, and the magnetic field direction, while still varying, is much less radial than at PSP perihelia.

The Parker-spiral average magnetic field (Parker 1958) organizes the baseline trend of these angles with varying radial distance. However, for PSP's closest approaches to the Sun, both the flow and the magnetic field are dominantly radial and PSP most often measures variations parallel to the magnetic field, yielding a deficit in measurements perpendicular to the



Original content from this work may be used under the terms of the [Creative Commons Attribution 4.0 licence](#). Any further distribution of this work must maintain attribution to the author(s) and the title of the work, journal citation and DOI.

magnetic field. This calls for care in interpretation of PSP observations, since the observed correlations may not be representative of the entire system. Here we examine separately the radial evolution of parallel and perpendicular energy-containing correlation scales. Parallel and perpendicular angular channels are chosen to correspond to angles  $0^\circ < \Theta_{\text{BV}} < 40^\circ$  and  $50^\circ < \Theta_{\text{BV}} < 90^\circ$ , respectively.

To expand the scope of the study, we employ observations by PSP, Helios 1, Advanced Composition Explorer (ACE), WIND, and Voyager 1. Previous studies have investigated the relationship between the parallel and perpendicular correlation scales ( $\lambda_C^{\parallel}$  and  $\lambda_C^{\perp}$ ). Ruiz et al. (2011) observed an anisotropy using Helios 1 data such that  $\lambda_C^{\parallel} < \lambda_C^{\perp}$ , whereas others (Matthaeus et al. 1990; Dasso et al. 2005; Weygand et al. 2011) reported that parallel lengths are greater near 1 au. More recently, PSP observes in its first five orbits that  $\lambda_C^{\parallel} < \lambda_C^{\perp}$  for heliocentric distances  $R < 0.30$  au (Bandyopadhyay & McComas 2021).

We are unable to study fast and slow wind intervals separately, with the exception of ACE and WIND data sets. The other data sets used in this study are dominated by slow wind ( $V_{\text{SW}} < 450 \text{ km s}^{-1}$ ), yielding weak statistical significance for results in fast wind ( $V_{\text{SW}} > 600 \text{ km s}^{-1}$ ). With this limitation in mind, we find evidence for the isotropization of  $\lambda_C^{\parallel}$  and  $\lambda_C^{\perp}$  with increasing  $R$ . Once isotropy is achieved, it continues to evolve depending on system dynamics causing temporary deviations; however, we cannot confidently comment on this evolution beyond 1 au due to weak statistical significance of parallel intervals observed by Voyager 1. In Section 2, we explain the methods used to compute the correlation length. Afterwards, we present the radial evolution of the winding angle and correlation lengths in Sections 3 and 4, respectively, with further discussion in Section 5. We include instrumentation and data specifics in Appendix.

## 2. Autocorrelation Method

We define magnetic field fluctuations  $\mathbf{b}$  by subtracting the averaged magnetic field from the total magnetic field  $\mathbf{B} - \langle \mathbf{B} \rangle$ , where  $\langle \cdot \rangle$  refers to a temporal average over an appropriately sized interval. For interval duration information, see Appendix. The Taylor “frozen-in” hypothesis (TH; Taylor 1938) implicitly associates a temporal lag  $\tau$  with a spatial lag  $\ell$  according to  $\ell = V_{\text{SW}}\tau$ , where  $V_{\text{SW}}$  is the bulk flow speed in the spacecraft frame, computed over a specified averaging interval. This approximate conversion from temporal to spatial lags is expected to be accurate when  $V_{\text{SW}}$  is large compared to characteristic speeds of the local fluctuation dynamics, such as the rms fluctuation speed or Alfvén speed  $V_A = B/\sqrt{4\pi\rho_i}$ , where  $B$  is the magnetic-field vector magnitude and  $\rho_i$  is the ion mass density. At distances near PSP perihelia,  $V_{\text{SW}}$  is comparable to  $V_A$ , weakening the validity of TH (Chhiber et al. 2019; Perez et al. 2021). In this study,  $\sim 1\%$  of PSP intervals (see Appendix), encompassing only radial distances  $R < 0.20$  au, exhibit  $V_A/V_{\text{SW}} > 0.66$ , which we considered to be poor validity of TH. Only  $\sim 0.10\%$  of intervals have  $V_A/V_{\text{SW}} > 1$ . Therefore, TH remains at either intermediate or high validity for the large majority of this study.

The two-time autocorrelation function  $R_C(\tau)$  of time-stationary magnetic-field fluctuations is defined as

$$R_C(\tau) = \frac{\langle \mathbf{b}(t) \cdot \mathbf{b}(t + \tau) \rangle}{\langle \mathbf{b}(t) \cdot \mathbf{b}(t) \rangle}. \quad (1)$$

The correlation time  $\tau_e$  is the characteristic time separation over which the fluctuations become uncorrelated. Here we identify  $\tau_e$  with the “e-folding” time, i.e.,  $R_C(\tau = \tau_e) = 1/e$ . This correlation time corresponds to the size of the energy-containing eddies, within the interval used for computation. Here TH is used to convert  $\tau_e$  to a spatial correlation scale, such that  $\lambda_C = V_{\text{SW}}\tau_e$ .

For all spacecraft in this study, with the exception of ACE, we use this method to estimate  $\lambda_C$ . For ACE, we employ  $\lambda_C$  values obtained from Roy et al. (2021), and computed via exponential fit of the correlation function. A preliminary estimate  $\tau'_e$  of the correlation time is first obtained via the “e-folding” method, given by  $R(\tau'_e)/R(0) = 1/e$ . Then a linear least-squares fit to  $\log [R(\tau)/R(0)] \sim -\tau/\tau_e$  is performed over the interval  $\tau \in [0, \tau'_e/2]$  to compute  $\tau_e$ , which can be converted to a corresponding spatial scale  $\lambda_C$ , as above.

## 3. Radial Distribution of the Alignment Angle

A key parameter in this study is the angle between the magnetic-field and flow velocity vectors, denoted  $\Theta_{\text{BV}}$ . In most cases, the radial velocity component dominates the tangential and normal components, thus motivating an approximation, and simplification, of this alignment angle when appropriate. This approximation leads to the winding angle  $\Theta_{\text{BR}}$  representing the angle between the magnetic-field and radial unit vectors defined as

$$\Theta_{\text{BR}} = \cos^{-1} \left( \frac{\langle |B_R| \rangle}{\langle \|B\| \rangle} \right), \quad (2)$$

where  $B_R$  is the radial component of the magnetic field  $\mathbf{B}$  in a heliocentric RTN coordinate system (Franz & Harper 2002),  $|\cdot|$  is an absolute value, and  $\|\cdot\|$  is a vector magnitude. The winding angle may also be referred to as the alignment angle for convenience. Taking the absolute value of  $B_R$  is necessary to avoid its average from vanishing in intervals that include crossings of the heliospheric current sheet (HCS) with an associated polarity reversal. If this operation is not performed prior to averaging then an interval with an HCS crossing may be improperly labeled as a perpendicular interval.

For ACE, WIND, and Voyager 1, it is sufficient to examine  $\Theta_{\text{BR}}$  since the observed direction of the flow is dominantly radial and spacecraft speeds are negligible compared to the bulk flow speed. However in PSP data the spacecraft velocity and the tangential component of the solar wind velocity can be comparable to the radial component of the latter (Fox et al. 2016; Kasper et al. 2019), so the angle between the magnetic field and the sampling direction is no longer well represented by  $\Theta_{\text{BR}}$ . Therefore, we compute  $\Theta_{\text{BV}}$  directly, defined as

$$\Theta_{\text{BV}} = \cos^{-1} \left( \frac{\langle |\mathbf{B}| \rangle \cdot \langle \mathbf{V}_{\text{SW}} \rangle}{\langle \|B\| \rangle \langle \|V_{\text{SW}}\| \rangle} \right), \quad (3)$$

where  $V_{\text{SW}}$  is the solar wind velocity measured in the spacecraft frame. For any intervals in which the computation of  $\Theta_{\text{BV}}$  is not possible (due to missing velocity data), then  $\Theta_{\text{BR}}$  will be

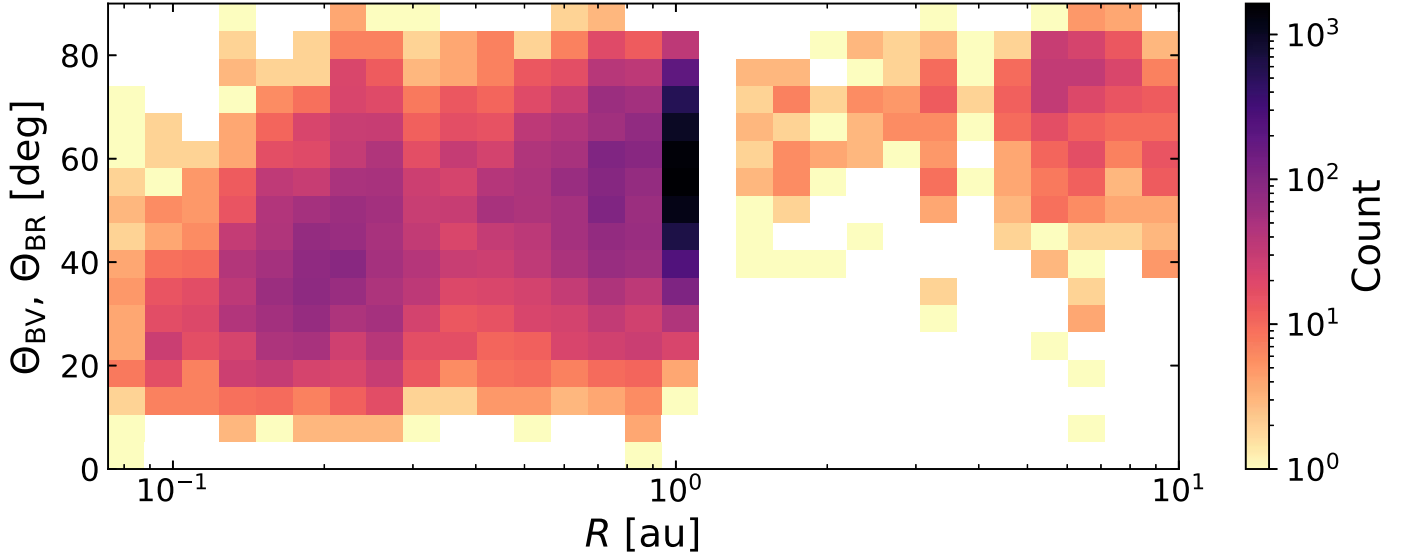


**Figure 1.** Radial distributions of alignment angle  $\Theta_{BV}$  for PSP and  $\Theta_{BR}$  for ACE, WIND, and Voyager 1. PSP interval sizes are 1 and 3 hr for heliocentric distances  $R < 0.3$  au and  $0.3 \text{ au} < R < 1$  au, respectively. Single day intervals are used for ACE, WIND, and Voyager 1 for  $R \geq 1$  au. Interval count of each bin is keyed to the color bar. White bins denote zero count.

used instead. Additionally, we constrain the alignment angles to lie in the range between  $0^\circ$  and  $90^\circ$  by not distinguishing between parallel or antiparallel.

The radial distributions of alignment angles are presented in Figure 1 for all spacecraft excluding Helios 1.<sup>5</sup> The count in each bin is keyed to the color bar. We observe a radially increasing alignment angle, corresponding to increasing central density in vertical slices. This is consistent with the mean Parker-spiral magnetic field. We have sufficient coverage of both angular channels,  $0^\circ < \Theta_{BV} < 40^\circ$  and  $50^\circ < \Theta_{BV} < 90^\circ$ , for  $R < 1$  au. However, Voyager 1 has a narrower range of angular coverage, since the mean Parker-spiral magnetic field forms an increasingly large angle relative to the radial (flow) direction, at those distances.

#### 4. Radial Variation of Parallel and Perpendicular Correlation Lengths

Using results from PSP, Helios 1, ACE, WIND, and Voyager 1, we compare the evolution of perpendicular and parallel correlation lengths from  $\sim 0.08$  au ( $16 R_\odot$ ) to 10 au. We illustrate the results in Figure 2. The top row of panels shows the radial variation of  $\lambda_C^\parallel$  and  $\lambda_C^\perp$ ; the bottom row of panels shows averages of these quantities within radial bins equally spaced in  $\log R$ . The density of blue and red points (top) demonstrates the transition from dominant-parallel sampling close to the Sun to dominant-perpendicular sampling above 1 au, as also seen in Figure 1. Both correlation scales systematically increase with  $R$  by nearly two orders of magnitude from  $\sim 5 \times 10^4$  km at 0.10 au to  $\sim 3 \times 10^6$  km at 10 au. The values between 0.40 and 5 au are consistent with previous work using Helios, ACE, and Ulysses observations (Ruiz et al. 2014). The increase in  $\lambda_C$  reflects the “aging” of turbulence, with larger scales participating in the turbulent cascade as the solar wind evolves (Matthaeus et al. 1998; Bruno & Carbone 2013) and flux tubes expand (Hollweg 1986).

<sup>5</sup> Ruiz et al. (2011) show the angles between the magnetic-field and flow vectors for Helios 1; however, their parallel and perpendicular angular channels are narrower than those used in the present study.

Radial power-law fits are presented in Table 2. The discontinuity at  $R = 0.30$  au is due to a shift from a 1 to 3 hr interval duration. The effect of interval size on the correlation scale is well known (Isaacs et al. 2015) and can also be seen at the 1 au boundary between PSP and ACE/WIND data, where we change from 3 hr to 1 day intervals.

For a quantitative examination of the radial evolution of anisotropy, we compute  $\langle \lambda_C^\parallel \rangle / \langle \lambda_C^\perp \rangle$ , where each of the correlation scales are first radially averaged in bins of size 0.10 au, for  $R \leq 1$  au. These accumulated averages are shown in Figure 3, which demonstrates the radial evolution of the observed anisotropy in the inner heliosphere. Data above 1 au are not shown because parallel intervals have low statistical weight. Nevertheless, for the full collection of samples beyond 1 au, we compute an overall average value  $\langle \lambda_C^\parallel \rangle / \langle \lambda_C^\perp \rangle \approx 0.97 \pm 0.17$  for the heliocentric distances covered by Voyager 1. Therefore, we observe a continued evolution in the outer heliosphere that may be characterized as either mild anisotropy or approximate isotropy.

Figure 3 shows that a trend toward increasing anisotropy develops below  $\approx 0.4$  au, with  $\lambda_C^\parallel < \lambda_C^\perp$ . This result, also seen by Bandyopadhyay & McComas (2021), appears superficially to be in contrast to interpretations of images obtained by STEREO (DeForest et al. 2016) that demonstrate a transition from striated thread-like morphology to more isotropic flocculated patterns. Normally, one would interpret striated structures as having longer parallel correlations. Indeed, it has been argued that this transition from coronal quasi-two-dimensional structure (Zank et al. 2021) to more isotropic turbulence outside the Alfvén critical zone is driven by dynamics of microstream shears (Ruffolo et al. 2020). However, we note that the length scales associated with the striation–flocculation transition in DeForest et al. (2016) correspond to lengths a decade larger than those we examine here with in situ measurements. It was already noted by DeForest et al. (2016) that structures at the correlation scale are much smaller than structure detected in the imaging studies. Therefore, there is no direct contradiction, though the origins of an initially very small parallel correlation scales remains

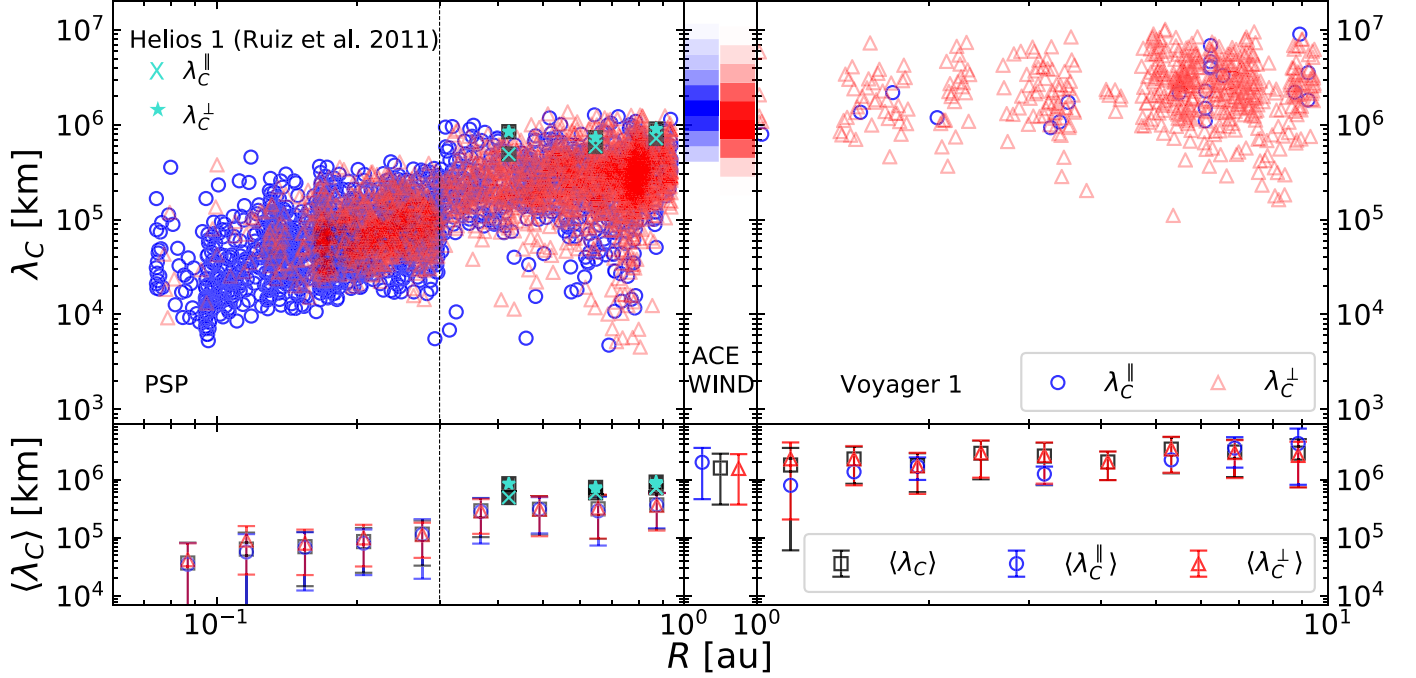


**Figure 2.** Correlation lengths observed by PSP and Helios 1 (left), ACE and WIND (middle), and Voyager 1 (right), vs. heliocentric distance. (Top) Results for individual intervals. (Bottom) Binned averages with bars representing standard deviation about mean. Blue circles, red triangles, and black squares represent parallel, perpendicular, and all intervals, respectively. Helios 1 data represented by three turquoise crosses ( $\lambda_C^{\parallel}$ ) and stars ( $\lambda_C^{\perp}$ ) are extracted from Ruiz et al. (2011). PSP data to left and right of the vertical dashed line at 0.3 au represent 1 hr and 3 hr interval sizes, respectively. Columns at  $\sim 1$  au represent number density (darker shades = larger counts) of 1 day intervals for ACE and WIND grouped as  $\lambda_C^{\parallel}$  (left, blue) and  $\lambda_C^{\perp}$  (right, red). Statistics of these distributions are in Table 1. Power-law fits for  $\lambda_C$ ,  $\lambda_C^{\parallel}$ , and  $\lambda_C^{\perp}$  are in Table 2.

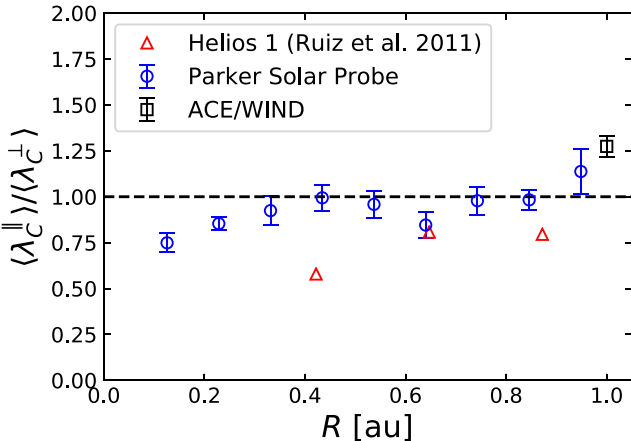


**Figure 3.** Ratios of  $\langle \lambda_C^{\parallel} \rangle / \langle \lambda_C^{\perp} \rangle$  for PSP (blue circles), Helios 1 (red triangles), and ACE/WIND (black square). Points represent radially binned averages of results presented in Figure 2. The statistics of the distribution from ACE/WIND are given in Table 1. Error bars represent standard error of the mean,  $\sigma / \sqrt{n}$ , where  $\sigma$  is standard deviation and  $n$  is number of samples. We also compute an average ratio  $\langle \lambda_C^{\parallel} \rangle / \langle \lambda_C^{\perp} \rangle \approx 0.97$  over all Voyager data out to 10 au, with 0.17 standard error.

unexplained. This contrast represents a possible change of symmetry between the ultra-large fluctuations that are just beginning to interact in the STEREO images, and the more strongly coupled nonlinear cascade that begins at the correlation scale. We await the refinements of the PUNCH mission (Deforest et al. 2021) that will span these ranges direct through improved imaging.

The picture that emerges is of a faster increase of  $\lambda_C^{\parallel}$  up to  $\approx 0.40$  au, which can be observed in Figure 3. Possible

**Table 1**  
Combined ACE and WIND Statistics for  $\lambda_C^{\parallel}$  and  $\lambda_C^{\perp}$ , Differentiated by Wind Speed

	$\langle \lambda_C^{\parallel} \rangle (10^6 \text{ km})$	$\langle \lambda_C^{\perp} \rangle (10^6 \text{ km})$	$\langle \lambda_C^{\parallel} \rangle / \langle \lambda_C^{\perp} \rangle$
All $V_{\text{SW}}$	$1.98 \pm 0.09$	$1.55 \pm 0.02$	$1.28 \pm 0.06$
$V_{\text{SW}} < 450 \text{ km/s}$	$1.98 \pm 0.11$	$1.67 \pm 0.02$	$1.19 \pm 0.07$
$V_{\text{SW}} > 600 \text{ km/s}$	$1.78 \pm 0.31$	$1.05 \pm 0.05$	$1.70 \pm 0.31$

**Note.** Values represent the mean value along with standard error of the mean,  $\sigma / \sqrt{n}$ , where  $\sigma$  is standard deviation and  $n$  is number of samples.

reasons for this more rapid increase in  $\lambda_C^{\parallel}$  compared to  $\lambda_C^{\perp}$  are discussed in greater detail in Section 5.

After attaining isotropy near 0.40 au, the turbulence continues to evolve with increasing radius, with some variation toward lower  $\lambda_C^{\parallel}$  near 0.60 au. The ratio then attains isotropy again by 0.8 au and increases such that  $\lambda_C^{\parallel} > \lambda_C^{\perp}$  near 1 au. This situation persists at 1 au where similar results are observed in ACE and WIND data. Table 1 shows averages and standard deviations of the ACE and WIND observations that are shown as distributions in Figure 2. Dasso et al. (2005) report that  $\langle \lambda_C^{\parallel} \rangle / \langle \lambda_C^{\perp} \rangle = 0.71$  for  $V_{\text{SW}} > 600 \text{ km s}^{-1}$  and  $\langle \lambda_C^{\parallel} \rangle / \langle \lambda_C^{\perp} \rangle = 1.18$  for  $V_{\text{SW}} < 450 \text{ km s}^{-1}$ . We report in Table 1 similar values to those of Dasso et al. (2005) for slow wind but not for fast wind. A possible reason for the inconsistency in the fast wind ratio lies in the differences in methods of computing  $\lambda_C^{\parallel}$  and  $\lambda_C^{\perp}$ .

We provide individual radial power-law fits to results from Figure 2; these are shown in Table 2 for different ranges of heliocentric distance. The more rapid radial evolution of  $\lambda_C^{\parallel}$  is reflected by the larger power-law exponents. Once  $\lambda_C^{\parallel}$  catches up to  $\lambda_C^{\perp}$ , isotropy is roughly maintained, as can be interpreted

**Table 2**  
Radial Power-law Fits to  $\lambda_C$ ,  $\lambda_C^{\parallel}$ , and  $\lambda_C^{\perp}$  from Figure 2

$\lambda_C \sim R^{\alpha \pm \sigma}$	$R < 0.30$ au	$0.30 \text{ au} < R < 1.0$ au	$R > 1$ au
$\lambda_C$	$0.97 \pm 0.04$	$0.29 \pm 0.01$	$0.27 \pm 0.01$
$\lambda_C^{\parallel}$	$1.03 \pm 0.06$	$0.28 \pm 0.03$	$0.64 \pm 0.12$
$\lambda_C^{\perp}$	$0.61 \pm 0.06$	$0.27 \pm 0.02$	$0.23 \pm 0.01$

**Note.** Quantities represent fitted parameters  $\alpha$  with standard deviation  $\sigma$  about the best fit.

by the combination of nearly equal power-law exponents for  $\lambda_C^{\parallel}$  and  $\lambda_C^{\perp}$  as well as their similar radial scaling for radial distances  $0.30 \text{ au} < R < 1$  au.

The connection between PSP and ACE/WIND and their general consistency presented in Figures 2 and 3 suggest a reversal of the initial anisotropy at radial distances within 0.40 au. The combined ACE/WIND ratio  $\langle \lambda_C^{\parallel} \rangle / \langle \lambda_C^{\perp} \rangle > 1$  for all  $V_{SW}$  conditions given in Table 1 confirms this observation. However, whether this reversal of the initial anisotropy is preserved past 1 au, or is just a temporary deviation from isotropy, remains inconclusive. One might presume from the radial scalings in Table 2 for radial distances beyond 1 au that  $\lambda_C^{\parallel}$  continues to grow past the perpendicular scale. However, no strong conclusion can be drawn from the available data since very few parallel intervals are found in the Voyager data. Pickup ions are also expected to affect  $\lambda_C^{\parallel}$  above 5 au (Zank et al. 2017).

## 5. Discussion

Data from the first eight PSP encounters reveals an anisotropy with  $\lambda_C^{\parallel} < \lambda_C^{\perp}$  at  $\sim 0.08$  au, also observed by Bandyopadhyay & McComas (2021). This is likely explained by the physical size of granulated cells on the Sun’s surface. The parallel scale is more dependent on the nature of the mechanisms that inject magnetic energy along the radial component of the magnetic field in the corona. In this regard it is possible to develop arguments (Matthaeus et al. 1990; Zank et al. 2021) of a general nature that the scale of energy injection relative to the magnetic field exerts a strong influence on the corresponding correlation scales. This reasoning may well explain the anisotropy observed in the inner heliosphere but there are no observations or detailed theories as yet that firmly establish this connection.

As one moves outward to  $\sim 0.40$  au,  $\lambda_C^{\parallel}$  and  $\lambda_C^{\perp}$  isotropize. A deviation from isotropy occurs once the solar wind reaches 1 au, as observed by PSP, ACE, and WIND. Near 1 au, a reversal of the initial anisotropy is observed, such that the parallel correlation scale becomes the larger of the two, with  $\lambda_C^{\parallel} / \lambda_C^{\perp} = 1.28$  (see Table 1). This is consistent with the observations by Dasso et al. (2005).

The trend toward greater  $\lambda_C^{\parallel} / \lambda_C^{\perp}$  at 1 au and beyond might be interpreted in at least two different ways:

(1) The anisotropy at 1 au represents a temporary deviation from the isotropy achieved at  $\approx 0.40$  au. As a result, for heliocentric distances beyond 1 au,  $\lambda_C^{\parallel} / \lambda_C^{\perp}$  remains  $\approx 1$ , even as other transient deviations occur, as seen in Figure 2. We note that turbulent MHD simulations support this view, finding that, after a startup transient that lasts several nonlinear times, the MHD system settles into a regime in which the correlation scale ratio remains roughly constant with values not far from

unity (Bandyopadhyay et al. 2019). Analysis of turbulence “aging” in the solar wind (Matthaeus et al. 1998) indicates that this condition should be well fulfilled within 1 au and beyond (see also Chhiber et al. 2016).

(2) The anisotropy at 1 au marks a change in system dynamics that causes a more rapid increasing in  $\lambda_C^{\parallel}$  relative to  $\lambda_C^{\perp}$  beyond 1 au. This can be supported by radial power-law fits yielding a stronger radial dependence in  $\lambda_C^{\parallel}$ . A caveat for both these possibilities is the weak statistical weight of parallel intervals from Voyager 1. Therefore, we cannot draw any strong conclusions from the evolution of  $\lambda_C^{\parallel} / \lambda_C^{\perp}$  beyond 1 au.

A stronger basis for conclusions may emerge from analysis of the more populated data intervals in the range between  $0.80 \text{ au} < R < 1$  au where one observes anisotropy increasing with radial distance. For example, there is ample evidence that solar wind turbulence has not yet attained a fully developed character in the inner heliosphere where there is evidence of increasing small-scale intermittency with increasing heliocentric distance (Alberti et al. 2020; Telloni et al. 2021; Cuesta et al. 2022; Sioulas et al. 2022). However, near 1 au, the rate of increase of intermittency reverses and decreases moving toward larger radial distances (Parashar et al. 2019; Cuesta et al. 2022). If the solar wind is still evolving toward fully developed status near 1 au, then the outer-scale anisotropy—what we have characterized by measuring  $\lambda_C^{\parallel} / \lambda_C^{\perp}$  beyond 1 au, may also still be evolving. In this sense the trend just inside of 1 au may represent the relatively slower evolution toward a weakly quasi-two-dimensional state. Such anisotropy may be the consequence of enhanced formation of perpendicular gradients relative to the large-scale magnetic-field direction (Shebalin et al. 1983), even if that familiar anisotropy is more often associated with inertial range scales where the effect is of greater magnitude than the moderate departure from isotropy observed here in the outer heliosphere beyond 1 au.

Future PSP orbits will provide the opportunity to examine the evolution of turbulence correlations closer to the Sun’s surface. The magnetic field direction and the solar wind direction are expected to be principally radial at the lower altitudes, so most observations will be of the parallel type, when standard Taylor hypothesis is applicable. However lower solar wind speed, higher Alfvén speed, and rapid spacecraft motion across the radial direction near perihelion may permit valuable studies of correlation anisotropy to be carried out using modified forms of the Taylor hypothesis (Matthaeus 1997; Klein et al. 2015; Perez et al. 2021). Large tangential velocities in the bulk flow close to the Sun (Weber & Davis 1967; Kasper et al. 2019) may also permit evaluation of perpendicular correlations below the Alfvén transition region (Chhiber et al. 2022).

Finally we remark, concerning the fundamental limitation of the present study, that for a single spacecraft analysis, it is not possible to simultaneously sample perpendicular and parallel correlations. Even with this limitation, the above analysis offers some interesting conclusions while also raising additional questions concerning the original evolution of correlation anisotropy in the solar wind. In any case, a more complete study of correlation anisotropy requires a multispacecraft mission that enables simultaneous measurements at varying angles, thus eliminating the influence on the results of variation of ambient conditions. We anticipate that the Helioswarm mission (Spence & Klein 2021) will provide refined answers to

these and related questions about the state and evolution of interplanetary turbulence.

This research is partially supported by NASA under the Heliospheric Supporting Research program grants 80NSSC18K1210 and 80NSSC18K1648, by the Parker Solar Probe Guest Investigator program 80NSSC21K1765 at Delaware and 80NSSC21K1767 at Princeton, and by Heliophysics Guest Investigator program 80NSSC19K0284, the PSP/IS $\odot$ IS Theory and Modeling project (Princeton subcontract SUB0000165), the IMAP Project under Princeton subcontract SUB0000317, and the PUNCH project under subcontract NASA/SWRI N99054DS.

## Appendix A Instrumentation and Data Description

**PSP.** Level 2 magnetic-field and Level 3 plasma data were extracted from NASA Goddard Space Flight Center Space Physics Data Facility (SPDF) in heliocentric RTN coordinates at full cadence. We use measurements made by the fluxgate magnetometer on board the FIELDS instrument suite (Bale et al. 2016) and by the Solar Probe Cup (SPC) on board the Solar Wind Electrons Alphas and Protons (SWEPAP) instrument (Kasper et al. 2016). We use available data from the first eight orbits, resampled as needed to the desired resolution of 1 s. These data cover the time period between 2018 October 5 to 2021 June 30. Interval sizes vary by heliocentric distance, such that 1 hr and 3 hr intervals are used for  $R < 0.30$  au and  $R > 0.30$  au, respectively (see discussion below). A Hampel filter is applied to proton velocity components in real space to remove large outliers. For a definition of this Hampel filter, see Pearson (2002) and Bandyopadhyay et al. (2018). When the solar wind speed in any PSP interval was unavailable due to data quality issues, speeds were linearly interpolated using nearby intervals in order to maximize the number of intervals for which a correlation time can be converted to length via the Taylor hypothesis.

**ACE.** Magnetic-field data was extracted from SPDF in RTN coordinates at a 1 s resolution for all available times from 1998 February 5 to 2008 March 30. The 1 s resolution data were resampled via an averaging technique to a 1 minute resolution. The twin triaxial fluxgate magnetometer on board ACE (Smith et al. 1998) provides magnetic field data and the Solar Wind Electron Proton Alpha Monitor instrument suite (McComas et al. 1998) provides plasma data. An interval size of 1 day is utilized. From a total of 3707 intervals, 3576 intervals were useful. Here, a useful interval is defined to have no more than 80% missing data.

**WIND.** Magnetic-field data were extracted from SPDF in RTN coordinates at a 1 minute resolution for all available times from 1998 February 5 to 2008 February 5. The Solar Wind Experiment (Ogilvie et al. 1995) provides plasma data and the Magnetic Field Investigation instrument suite (Lepping et al. 1995) provides magnetic field data via a boom-mounted dual triaxial fluxgate magnetometer. An interval size of 1 day is utilized. From a total of 3650 intervals, 3626 intervals were useful.

**Voyager 1.** The existing archival Voyager 1 magnetic field data were extracted from SPDF in RTN coordinates at a 1.92s resolution. Data covers heliocentric distances ranging from 1 to 10 au. The Voyager mission used a dual low-field and high-field magnetometer system (Behannon et al. 1977) for

magnetic-field measurements, and the onboard plasma instrument (Bridge et al. 1977) for other plasma parameters such as bulk flow speed and proton density. Although missing data and data gaps were encountered, we discovered several other inaccuracies with respect to the quality of the data, all of which were resolved (Cuesta 2020; Cuesta et al. 2022). The improved data set is publicly available at <https://doi.org/10.5281/zenodo.5711177>. An interval size of 1 day is applied to all heliocentric distances covered by Voyager 1. From a total of 1333 intervals, 780 intervals were useful.

**Computation specifics.** Helios 1 results presented in this study were extracted from Ruiz et al. (2011). Results will not reflect selections of fast and slow solar wind, with the exception of reported statistics of combined ACE and WIND intervals given in Table 1. We obtained  $\lambda_C^{\parallel}$  and  $\lambda_C^{\perp}$  from intervals with alignment angles assigned to the angular channels of  $0^\circ < \Theta < 40^\circ$  (parallel channel) and  $50^\circ < \Theta < 90^\circ$  (perpendicular channel), respectively. When narrowing the angular ranges for parallel and perpendicular classifications by  $10^\circ$ , the results remain nearly the same. Further narrowing of the angular ranges produces large statistical uncertainties.

Finally, we discuss the interval sizes used in this study. For turbulence analyses, an interval size containing several correlation scales is ideal. Further, the interval should not be so large that solar rotation effects are included. From Isaacs et al. (2015), the optimized averaging window for computing correlation scales was determined to be between 10 and 20 hr long at 1 au. Therefore, we decided that 1 day interval lengths were most suitable when computing correlation lengths for ACE, WIND, and Voyager 1. For PSP, we selected a boundary at 0.30 au to correspond to a shift from 1 to 3 hr intervals with increasing heliocentric distance. The smaller intervals reflect the decreasing correlation scales with a decrease in heliocentric distance (Chhiber et al. 2021); the average correlation time at about 0.10 au is  $\approx 6$  minutes, which allows for the minimum required oversampling (Isaacs et al. 2015). Additionally, closer to the Sun, the local magnetic field is dominantly radial resulting in less opportunities to find longer intervals having perpendicular alignment angles. In order to obtain more statistical weight of perpendicular intervals at PSP perihelia, 1 hr interval times were selected (see also Bandyopadhyay et al. 2022).

## ORCID iDs

- Manuel Enrique Cuesta  <https://orcid.org/0000-0002-7341-2992>
- Rohit Chhiber  <https://orcid.org/0000-0002-7174-6948>
- Sohom Roy  <https://orcid.org/0000-0003-3891-5495>
- Joshua Goodwill  <https://orcid.org/0000-0002-5354-1164>
- Francesco Pecora  <https://orcid.org/0000-0003-4168-590X>
- William H. Matthaeus  <https://orcid.org/0000-0001-7224-6024>
- Tulasi N. Parashar  <https://orcid.org/0000-0003-0602-8381>
- Riddhi Bandyopadhyay  <https://orcid.org/0000-0002-6962-0959>

## References

- Alberti, T., Laurenza, M., Consolini, G., et al. 2020, *ApJ*, 902, 84
- Bale, S. D., Goetz, K., Harvey, P. R., et al. 2016, *SSRV*, 204, 49
- Bandyopadhyay, R., Chasapis, A., Chhiber, R., et al. 2018, *ApJ*, 866, 81
- Bandyopadhyay, R., Matthaeus, W. H., McComas, D. J., et al. 2022, *ApJL*, 926, L1

Bandyopadhyay, R., Matthaeus, W. H., Oughton, S., & Wan, M. 2019, *JFM*, **876**, 5

Bandyopadhyay, R., & McComas, D. J. 2021, *ApJ*, **923**, 193

Behannon, K. W., Acuna, M. H., Burlaga, L. F., et al. 1977, *SSRv*, **21**, 235

Bridge, H., Belcher, J., Butler, R., et al. 1977, *SSRv*, **21**, 259

Bruno, R., & Carbone, V. 2013, *LRSP*, **10**, 2

Chhiber, R., Matthaeus, W. H., Oughton, S., & Parashar, T. N. 2020, *PhPl*, **27**, 062308

Chhiber, R., Matthaeus, W. H., Usmanov, A. V., Bandyopadhyay, R., & Goldstein, M. L. 2022, *MNRAS*, **513**, 159

Chhiber, R., Usmanov, A., Matthaeus, W., & Goldstein, M. 2016, *ApJ*, **821**, 34

Chhiber, R., Usmanov, A. V., Matthaeus, W. H., & Goldstein, M. L. 2021, *ApJ*, **923**, 89

Chhiber, R., Usmanov, A. V., Matthaeus, W. H., Parashar, T. N., & Goldstein, M. L. 2019, *ApJS*, **242**, 12

Cuesta, M. E. 2020, Master's thesis, University of Delaware

Cuesta, M. E., Parashar, T. N., Chhiber, R., & Matthaeus, W. H. 2022, *ApJS*, **259**, 23

Dasso, S., Milano, L. J., Matthaeus, W. H., & Smith, C. W. 2005, *ApJL*, **635**, L181

DeForest, C., Gibson, S., Killough, R., et al. 2021, *BAAS*, **53**, 313

DeForest, C. E., Matthaeus, W. H., Vialli, N. M., & Cranmer, S. R. 2016, *ApJ*, **828**, 66

Fox, N. J., Velli, M. C., Bale, S. D., et al. 2016, *SSRv*, **204**, 7

Franz, M., & Harper, D. 2002, *P&SS*, **50**, 217

Goldreich, P., & Sridhar, S. 1995, *ApJ*, **438**, 763

Hollweg, J. V. 1986, *JGR*, **91**, 4111

Isaacs, J. J., Tassein, J. A., & Matthaeus, W. H. 2015, *JGRA*, **120**, 868

Kasper, J., Bale, S., Belcher, J., et al. 2019, *Natur*, **576**, 228

Kasper, J. C., Abiad, R., Austin, G., et al. 2016, *SSRv*, **204**, 131

Klein, K. G., Perez, J. C., Verscharen, D., Mallet, A., & Chandran, B. D. G. 2015, *ApJL*, **801**, L18

Lepping, R. P., Acuña, M. H., Burlaga, L. F., et al. 1995, *SSRv*, **71**, 207

Matthaeus, W. H. 1997, in AIP Conf. Ser. 385, Robotic Exploration Close to the Sun: Scientific Basis, ed. S. R. Habbal (New York: AIP), 67

Matthaeus, W. H., Goldstein, M. L., & Roberts, D. A. 1990, *JGR*, **95**, 20673

Matthaeus, W. H., Smith, C. W., & Oughton, S. 1998, *JGRA*, **103**, 6495

McComas, D. J., Bame, S. J., Barker, P., et al. 1998, *SSRv*, **86**, 563

Ogilvie, K. W., Chornay, D. J., Fritzenreiter, R. J., et al. 1995, *SSRv*, **71**, 55

Oughton, S., & Engelbrecht, N. E. 2021, *NewA*, **83**, 101507

Oughton, S., Matthaeus, W. H., Wan, M., & Osman, K. T. 2015, *RSPTA*, **373**, 20140152

Parashar, T. N., Cuesta, M., & Matthaeus, W. H. 2019, *ApJL*, **884**, L57

Parker, E. N. 1958, *ApJ*, **128**, 664

Pearson, R. K. 2002, *IEEE Transactions on Control Systems Technology*, **10**, 55

Perez, J. C., Bourouaine, S., Chen, C. H. K., & Raouafi, N. E. 2021, *A&A*, **650**, A22

Robinson, D. C., & Rusbridge, M. G. 1971, *PhFl*, **14**, 2499

Roy, S., Chhiber, R., Dasso, S., Ruiz, M. E., & Matthaeus, W. H. 2021, *ApJL*, **919**, L27

Ruffolo, D., Matthaeus, W. H., Chhiber, R., et al. 2020, *ApJ*, **902**, 94

Ruiz, M. E., Dasso, S., Matthaeus, W. H., Marsch, E., & Weygand, J. M. 2011, *JGRA*, **116**, A10102

Ruiz, M. E., Dasso, S., Matthaeus, W. H., & Weygand, J. M. 2014, *SoPh*, **289**, 3917

Shebalin, J. V., Matthaeus, W. H., & Montgomery, D. 1983, *JPIPh*, **29**, 525

Sioulas, N., Velli, M., Chhiber, R., et al. 2022, *ApJ*, **927**, 140

Smith, C. W., L'Heureux, J., Ness, N. F., et al. 1998, *SSRv*, **86**, 613

Spence, H., & Klein, K. 2021, in EGU General Assembly Conference Abstracts, HelioSwarm: The Nature of Turbulence in Space Plasmas, 23 (Göttingen: Copernicus), 12092

Taylor, G. I. 1938, *RSPSA*, **164**, 476

Telloni, D., Sorriso-Valvo, L., Woodham, L. D., et al. 2021, *ApJL*, **912**, L21

Weber, E. J., & Davis Leverett, J. 1967, *ApJ*, **148**, 217

Weygand, J. M., Matthaeus, W. H., Dasso, S., & Kivelson, M. G. 2011, *JGRA*, **116**, A08102

Zank, G. P., Adhikari, L., Hunana, P., et al. 2017, *ApJ*, **835**, 147

Zank, G. P., Zhao, L.-L., Adhikari, L., et al. 2021, *PhPl*, **28**, 080501